

## Multi-objective aerodynamic optimization design of high-speed train head shape<sup>\*</sup>

Liang ZHANG<sup>†</sup>, Ji-ye ZHANG, Tian LI, Ya-dong ZHANG

(State Key Laboratory of Traction Power, Southwest Jiaotong University, Chengdu 610031, China)

<sup>†</sup>E-mail: swjtu.zl@163.com

Received Dec. 6, 2016; Revision accepted Mar. 6, 2017; Crosschecked Oct. 12, 2017

**Abstract:** To improve the aerodynamic performance of high-speed trains (HSTs) running in the open air, a multi-objective aerodynamic optimization design method for the head shape of a HST is proposed in this paper. A parametric model of the HST was established and seven design variables of the head shape were extracted. Sample points and their exact values of optimization objectives were obtained by an optimal Latin hypercube sampling (opt. LHS) plan and computational fluid dynamic (CFD) simulations, respectively. A Kriging surrogate model was constructed based on the sample points and their optimization objectives. Taking the total aerodynamic drag force and the aerodynamic lift force of the tail coach as the optimization objectives, the multi-objective aerodynamic optimization design was performed based on a non-dominated sorting genetic algorithm-II (NSGA-II) and the Kriging model. After optimization, a series of Pareto-optimal head shapes were obtained. An optimal head shape was selected from the Pareto-optimal head shapes, and the aerodynamic performance of the HST with the optimal head shape was compared with that of the original train in conditions with and without crosswinds. Compared with the original train, the total aerodynamic drag force is reduced by 2.61% and the lift force of the tail coach is reduced by 9.90% in conditions without crosswind. Moreover, the optimal train benefits from lower fluctuations in aerodynamic loads in crosswind conditions.

**Key words:** High-speed trains (HSTs); Multi-objective optimization; Aerodynamic performance; Parametric model; Kriging model; Genetic algorithm (GA)

<http://dx.doi.org/10.1631/jzus.A1600764>

**CLC number:** U271.91; O355

### 1 Introduction

As a transport with high speed, low energy consumption and pollution, high-speed trains (HSTs) have been developed rapidly in recent decades (Smith and Zhou, 2014; Han *et al.*, 2015; Sone, 2015; Tan *et al.*, 2016). With the increase in train running speeds, aerodynamic problems become more and more prominent and significantly influence the operational safety of trains and the amenity of passengers (Raghunathan *et al.*, 2002; Schwanitz *et al.*, 2013; Zhai *et al.*, 2015). The aerodynamic drag force is

proportional to the square of the train running speed. When the train speed reaches 250–300 km/h, the aerodynamic drag force accounts for 75% of the total resistance (Brockie and Baker, 1990). Thus, the aerodynamic drag force becomes one of the main factors which restrain train speed and energy conservation. The aerodynamic lift force of the tail coach is also a key factor which affects the operational safety and amenity of HSTs. The aerodynamic uplift force may reduce the wheel-rail contact force, and an excessive uplift force could lead to derailment in extreme conditions. As a result, the reduction of the total aerodynamic drag force and the lift force of the tail coach is of great importance in the aerodynamic design of HSTs.

The streamlined head has a great effect on the aerodynamic performance of HSTs, and the

<sup>\*</sup> Project supported by the National Natural Science Foundation of China (Nos. 51475394 and 51605397) and the High-speed Railway Basic Research Fund Key Project of China (No. U1234208)

 ORCID: Liang ZHANG, <http://orcid.org/0000-0002-7403-7979>

© Zhejiang University and Springer-Verlag GmbH Germany 2017

aerodynamic performance can be effectively improved by the optimization of the head shape (Baker, 2010; Ding *et al.*, 2016). Many objectives need to be considered in the design of the head shape of HSTs, such as the aerodynamic drag force, aerodynamic lift force, crosswind stability, and aerodynamic noise (Baker, 2010; Li *et al.*, 2013; Xiao *et al.*, 2014; Thompson *et al.*, 2015). Many design parameters are needed to accurately describe the head shape of HSTs. Meanwhile, the aerodynamic shape optimization requires many flow field calculations. Therefore, it is very difficult to take into account all the design objectives in the optimization of the head shape of HSTs.

The traditional method for head shape design of HSTs is as follows: map out various head shapes, and then compare and select the best head shape by wind tunnel tests, moving model tests or numerical simulations (Yang *et al.*, 2012; Zhang and Zhou, 2013; Bell *et al.*, 2015). Essentially, the traditional method is an optimum seeking method which is heavily dependent on the engineering experience of the designers. The design period of the head shape of HSTs using the traditional method is very long. To overcome the disadvantages of the traditional method, the direct optimization method has been applied to the optimization of the head shape of HSTs in recent years. Direct optimization means using mathematical methods to seek optimal solutions of some design objectives while at the same time satisfying certain constraint conditions. In order to reduce the micro-pressure wave induced by a HST travelling through a tunnel, Lee and Kim (2007) performed an optimization of the train nose shape based on a Kriging model. Krajnović (2009) optimized a HST head to reduce the aerodynamic drag force and improve the crosswind stability of the train by using response surface methods. Sun *et al.* (2010) combined a genetic algorithm (GA) and an arbitrary shape deformation technique to optimize the head shape of a HST. Vytla *et al.* (2010) performed an optimization of a 2D train nose to minimize the aerodynamic drag and the aerodynamic noise based on a GA-particle swarm optimization (GA-PSO) hybrid algorithm and a Kriging model. Yu *et al.* (2013) optimized a simple 3D HST head by GA to reduce the aerodynamic drag and load reduction factor. Yao *et al.* (2012b; 2014) and Li *et al.* (2016) performed an optimization of a HST head using GA based on a Kriging model. Muñoz-paniagua

*et al.* (2014) conducted an optimization of the nose shape of a HST entering a tunnel by the application of GAs, aiming at minimizing the aerodynamic drag and the maximum micro-pressure wave. Yao *et al.* (2016) proposed an optimization approach to the HST nose by combining the support vector machines (SVMs) model and the particle swarm optimization (PSO) method.

In conclusion, the aerodynamic head shape optimizations of HSTs referred in the above literature mainly focused on 2D profiles or simple 3D shapes. Yao *et al.* (2012a) studied the aerodynamic drag distribution of a HST. Results showed that the aerodynamic drag of the bogies accounted for 27.4% of the total aerodynamic drag, and the aerodynamic drag of the bogie beneath the streamlined head of the head coach was significantly larger than that of the other bogies. Thus, a multi-objective optimization design of the head shape of a HST containing bogies is carried out in the present paper, and the bogie area beneath the streamlined head is optimized. The total aerodynamic drag coefficient ( $C_d$ ) and the aerodynamic lift coefficient ( $C_l$ ) of the tail coach are also set to be optimization objectives. A Kriging surrogate model is constructed to reduce the computational fluid dynamic (CFD) cost and improve the optimization efficiency. A series of Pareto-optimal head shapes are obtained by a multi-objective optimization based on a non-dominated sorting genetic algorithm-II (NSGA-II) and the Kriging surrogate model. An optimal head shape is selected from the Pareto-optimal head shapes, and its aerodynamic performance is compared with that of the original train in conditions with and without crosswinds.

## 2 Optimization design process

The optimization design process of the HST head shape in the present paper is listed as below (Fig. 1):

- (1) Determine the design variables and optimization objectives according to the optimization problems.

- (2) Establish the original train model and parameterize the streamlined head of the train.

(3) Design the initial samples in the design space by optimal Latin hypercube sampling (opt. LHS) plan, and deform the head shape based on the samples and the parametric model of the original train.

(4) Calculate the optimization objectives of the samples by CFD simulations.

(5) Construct the Kriging model based on the samples and their optimization objectives via GA and analyze the prediction accuracy of the Kriging model.

(6) Based on the Kriging model constructed in step (5), perform the multi-objective optimization of the HST head shape using NSGA-II, and obtain a series of Pareto-optimal head shapes.

(7) Pick out two head shapes randomly from the Pareto-optimal head shapes as the testing samples, and perform CFD calculations to judge whether the prediction accuracy has been achieved.

(8) If the prediction accuracy of the testing sample is not met, add the testing sample to the training samples, return to step (5), and reconstruct the Kriging model.

(9) If the prediction accuracy of the testing samples is met, the Kriging model is regarded as correctly constructed and the Pareto-optimal head shapes are the final optimal head shapes.

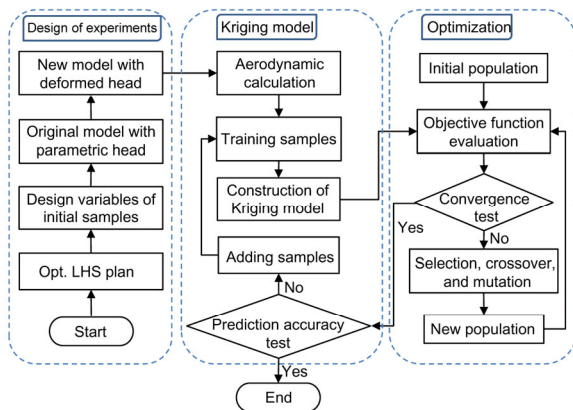


**Fig. 1** Schematic representation of the whole optimization design process

### 3 Parametric method of the train head

The 3D parametric model of the HST is established by the commercial software CATIA. The parametric method for the HST head mainly involves the following two aspects: (1) establishment of the original train model; (2) parameterization of the train head.

#### 3.1 Establishment of the original train model

As the train model has a good symmetry, only the left half portion of the head coach and the quarter portion of the middle coach need to be modelled. The whole train model with three coaches can be obtained by symmetry operations. In this study, a number of B-spline surfaces are used to describe the train surface. Fig. 2 shows the model of the left half head coach and a quarter of the middle coach. To facilitate the later description, the main control curves of the streamlined head are numbered C1 to C8, as shown in Fig. 3.

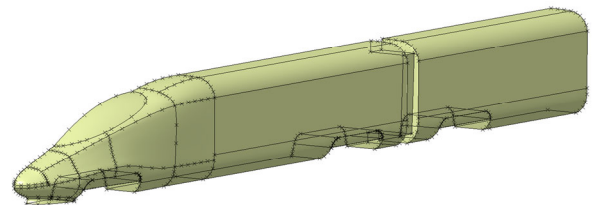


**Fig. 2** Model of the left half head coach and the quarter middle coach

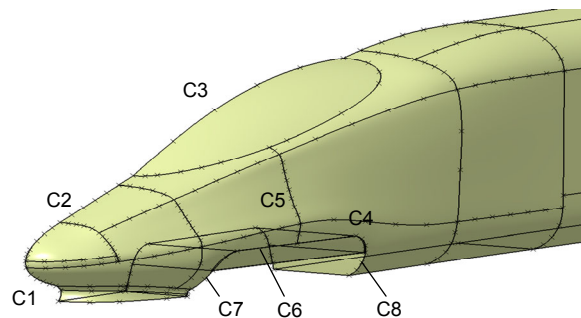


**Fig. 3** Numbers of the main control curves of the streamlined head

#### 3.2 Parameterization of the train head

Based on the original train model, the streamlined head of the HST is parameterized by a CATIA script file and a MATLAB code. The coordinates of the control points of the streamlined head are recorded in the CATIA script file, and then the deformation of the train head can be achieved by modifying the coordinates through the MATLAB code. As the length of the streamlined head and the maximum cross-sectional area of the train body have a great influence on the aerodynamic performance of HSTs, the length of the streamlined head and the maximum cross-sectional area are kept unchanged in the

optimization process. Seven design variables of the train head are extracted, i.e.,  $zs_1$ ,  $dz_2$ ,  $dz_3$ ,  $dy_4$ ,  $ys_5$ ,  $dy_6$ , and  $xs_7$ . The deformation functions of the main control curves are listed as follows:

$$z_n(i_1) = z_o(i_1) + zs_1(z_o(i_1) - z_o(1)), \quad (1)$$

$$i_1 = 1, 2, \dots, n_1,$$

where  $z$  is the  $z$  coordinate of the control point of C1, the subscripts  $n$  and  $o$  indicate the deformed control point and the original control point, respectively.  $i_1$  is the number of the control points of C1,  $zs_1$  is the design variable which controls the nose height, and  $n_1$  is the total number of the control points of C1.

The deformation forms of C2 and C3 are the same. Taking C2 as an example, the deformation function of C2 is shown below:

$$z_n(i_2) = z_o(i_2) + dz_2 \frac{x_o(i_2) - x_o(1)}{x_o(k_2) - x_o(1)}, \quad (2)$$

$$i_2 = 1, 2, \dots, k_2,$$

$$z_n(i_2) = z_o(i_2) + dz_2 \frac{x_o(i_2) - x_o(n_2)}{x_o(k_2) - x_o(n_2)}, \quad (3)$$

$$i_2 = k_2 + 1, k_2 + 2, \dots, n_2,$$

where  $x$  and  $z$  are the  $x$  and  $z$  coordinates of the control point of C2,  $i_2$  is the number of the control points of C2,  $dz_2$  is the design variable which controls the top height of the front hood,  $n_2$  is the total number of the control points of C2, and  $k_2$  is the number of the key control points of C2. The key control point of C2 is selected at the top point of the front hood, while the key control point of C3 is selected at the top point above the driver.

The deformation of C4 is given below:

$$y_n(i_4) = y_o(i_4) + dy_4 \frac{x_o(i_4) - x_o(1)}{x_o(k_4) - x_o(1)}, \quad (4)$$

$$i_4 = 1, 2, \dots, k_4,$$

$$y_n(i_4) = y_o(i_4) + dy_4 \frac{x_o(i_4) - x_o(n_4)}{x_o(k_4) - x_o(n_4)}, \quad (5)$$

$$i_4 = k_4 + 1, k_4 + 2, \dots, n_4,$$

where  $x$  and  $y$  are the  $x$  and  $y$  coordinates of the control point of C4.  $i_4$  is the number of the control points

of C4,  $dy_4$  is the design variable which controls the lateral width of the maximum horizontal control curve C4,  $n_4$  is the total number of the control points of C4.  $k_4$  is the number of the key control points of C4, which is selected in the middle of C4.

The deformation of C5 is given below:

$$y_n(i_5) = y_o(i_5) \times \left( \frac{ys_5(i_5 - 1)(n_5 - i_5)}{(i_5 - 1)(i_5 - 1) + (n_5 - i_5)(n_5 - i_5)} + 1 \right), \quad (6)$$

$$i_5 = 1, 2, \dots, n_5,$$

where  $y$  is the  $y$  coordinate of the control point of C5,  $i_5$  is the number of the control point of C5,  $ys_5$  is the design variable which controls the concave-convex degree of the auxiliary control curve C5, and  $n_5$  is the total number of the control points of C5.

The deformation of C6 is given below:

$$y_n(i_6) = y_o(i_6) + dy_6, \quad (7)$$

$$i_6 = 1, 2, \dots, n_6,$$

where  $y$  is the  $y$  coordinate of the control point of C6,  $i_6$  is the number of the control points of C6,  $dy_6$  is the design variable which controls the lateral width of the bogie area, and  $n_6$  is the total number of control points of C6.

The deformation forms of C7 and C8 are the same. Taking C7 as an example, the deformation function of C7 is shown below:

$$x_n(i_7) = x_o(1) + xs_7(x_o(i_7) - x_o(1)), \quad (8)$$

$$i_7 = 1, 2, \dots, n_7,$$

where  $x$  is the  $x$  coordinate of the control point of C7,  $i_7$  is the number of the control points of C7,  $xs_7$  is the design variable which controls the angle between the bogie area partition and the cross section, and  $n_7$  is the total number of the control points of C7.

The control curves are deformed one by one. Note that when the main control curves are deformed, the other control curves connected with them also need to be deformed to keep the train surface smooth and continuous. To meet the requirements of engineering applications, seven design variables are

restrained. The initial values and their ranges of the design variables are presented in Table 1.

## 4 Computational fluid dynamic method and validation

### 4.1 Numerical method

#### 4.1.1 Reynolds averaged Navier-Stokes method

In this study, the train running speed is 350 km/h. The Mach number is 0.286 in conditions without crosswind and is lower than 0.3, so air compressibility can be neglected. The 3D steady incompressible Reynolds averaged Navier-Stokes (RANS) equations are used to predict the aerodynamic forces and moments of the HSTs. The convective flux and temporal discretization are calculated using Roe's FDS scheme and lower-upper symmetric Gauss-Seidel (LU-SGS), respectively (Yao *et al.*, 2014). The  $k-\omega$  shear stress transport (SST) model is adopted as the turbulent model. The standard wall functions are used near the wall to ensure the accuracy of the CFD results with a limited amount of mesh.

#### 4.1.2 Detached Eddy simulation method

Compared with the steady calculation, the unsteady calculation is more time-consuming. However, there are significant unsteady aerodynamic characteristics of HSTs in crosswinds (Eichinger *et al.*, 2015; Zhang *et al.*, 2016). The unsteady aerodynamic performances of the original train and the optimal

train under crosswinds are studied using a detached Eddy simulation (DES) method based on the  $k-\omega$  SST turbulent model. The DES is a hybrid method which combines RANS and large Eddy simulation (LES) (Nishino *et al.*, 2008). This method is described briefly below: the near-wall regions are modelled with the help of the base RANS turbulent closure, in the separated flow regime; if the mesh is fine enough, a sub-grid scale model is used similar to the LES method. It is realized by replacing the turbulent length scale factor with the function  $\min[l, 0.65\Delta_{\max}]$ , in which  $l$  is the turbulent length scale factor, and  $\Delta_{\max}$  is the maximum length of the side of the controlling volume.

### 4.2 Computational model, domain, and boundary conditions

The train model used in the flow field calculation consists of the train body established in Section 3 and six bogies, as shown in Fig. 4. The geometric parameters of the train model are as follows: the length of the head coach and the tail coach is 27.5 m, the length of the middle coach is 25 m, and the shapes of the head coach and the tail coach are the same. The width and height of the train are 3.28 m and 3.8 m, respectively. The length of the streamlined head is 12 m, and the maximum cross-sectional area is 11.93 m<sup>2</sup>.

Fig. 5 shows the computational domain of the flow field. The distance between the bottom of the train body and the ground is 0.376 m. The computational domain has a uniform velocity of 97.22 m/s corresponding to the train running speed on the inlet

Table 1 Initial values and ranges of the design variables

Design variable	$zs_1$	$dz_2$ (mm)	$dz_3$ (mm)	$dy_4$ (mm)	$ys_5$	$dy_6$ (mm)	$xs_7$
Initial value	1.0	0	0	0	0.0	0	1.0
Lower bound	0.8	0	0	-30	-0.2	0	0.5
Upper bound	1.2	200	200	50	0.4	30	1.5

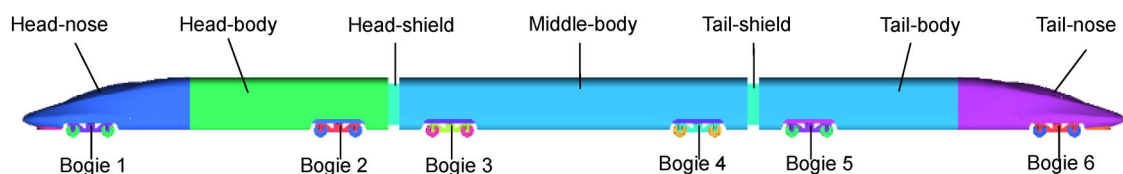


Fig. 4 Train model

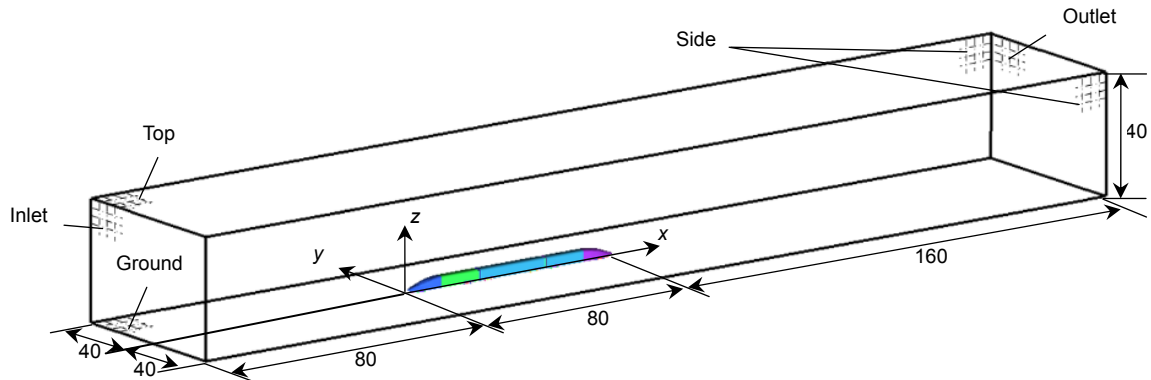


Fig. 5 Computational domain (unit: m)

boundary. The outlet of the computational domain is set as a pressure outlet boundary, and the pressure is specified as zero. The two sides and the top of the domain are set as symmetry boundaries. The train surface is set as a non-slip wall. In order to simulate the ground effect, the ground is set as a no-slip wall moving with the same speed as the inlet flow.

### 4.3 Computational mesh

The computational mesh is built using the software ICFM CFD, which consists of tetrahedral elements, with five prismatic cell layers near the train surface (growth rate of 1.2). Two refinement zones are defined around the train. To assess the influence of different spatial meshes on the calculation results, a mesh-independent validation is performed in the present paper. With the thickness of the first prismatic cell layer satisfying the requirement of the wall function ( $30 \leq y^+ \leq 50$ ), three sets of mesh are obtained by changing the surface mesh size of the train and the volume mesh size of the refinement zones. The computational results of the three sets of mesh are listed in Table 2. The aerodynamic load coefficients are calculated using the equations in (Yao *et al.*, 2014). It can be seen from Table 2 that little difference in the computational results of the second and the third sets of mesh could be observed, and the variations of the total aerodynamic drag coefficient and the lift coefficient of the tail coach are within 1%. Therefore, considering computational accuracy, the third set of mesh is adopted in the optimization. The mesh layout of the third set of mesh is as follows: the thickness of the first prismatic layer is 0.5 mm; the maximum surface

Table 2 Computational results of the three sets of mesh

Cells number ( $\times 10^6$ )	$C_d$ -total	$C_d$ -variation (%)	$C_l$ -tail	$C_l$ -variation (%)
16.91	0.3302	—	0.0912	—
25.98	0.3363	1.85	0.0938	2.80
31.23	0.3371	0.24	0.0939	0.14

mesh sizes of the streamlined head, train body, and bogies are 30 mm, 100 mm, and 30 mm, respectively. The maximum volume mesh sizes of the computational domain and refinement zones are 2000 mm and 100 mm, respectively. The total amount of the third set of mesh is 31.23 million. Fig. 6 shows the distributions of the partial mesh. As shown in Fig. 7, the values of  $y^+$  around the train surface are mainly in the range of 30 to 50.

### 4.4 CFD validation

The wind tunnel test model of a new type of HST is chosen for CFD validation. The train model is 1/8th scale and consists of three coaches (the head coach, the middle coach, and the tail coach). The measurements were conducted in the second test section of a 8 m $\times$ 6 m wind tunnel in China Aerodynamic Research and Development Center (CARDC). The aerodynamic drag forces and lift forces of the HST were measured by a six-component balance system. The wind tunnel test model and the numerical validation model are basically the same (Fig. 8).

The inlet wind speeds of the wind tunnel test and the numerical validation are all 55.56 m/s (200 km/h). The mesh layout method and numerical method used

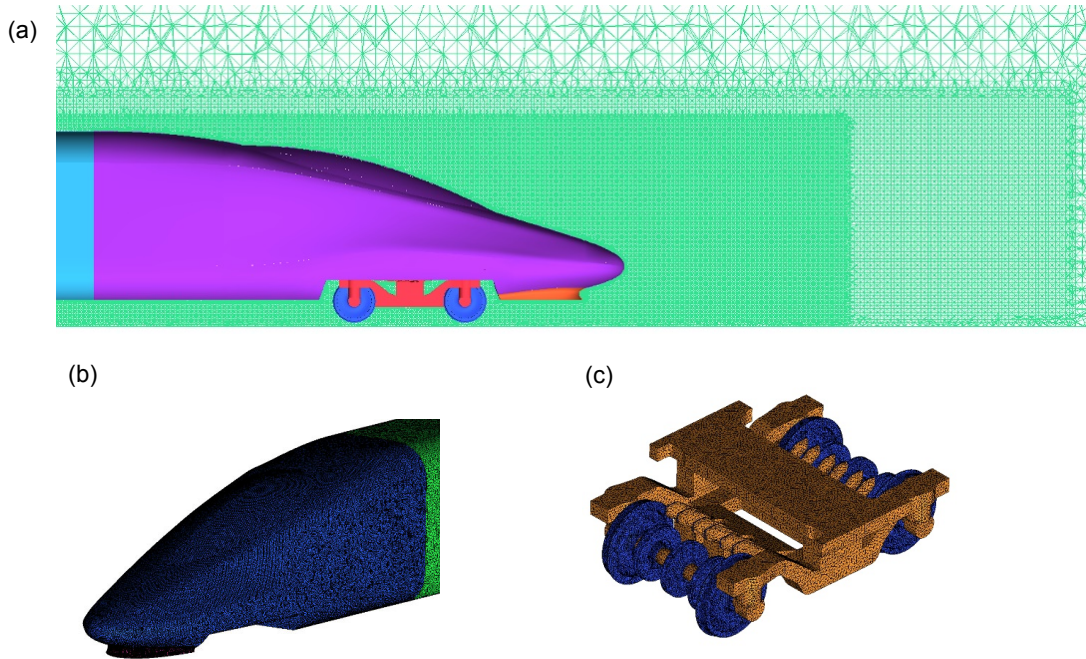


**Fig. 6 Representation of the partial mesh**

(a) Spatial mesh of the longitudinal symmetry section around the streamlined head of the tail coach; (b) Surface mesh of the streamlined head; (c) Surface mesh of the bogie



**Fig. 7 Values of  $y^+$  around the train surface**

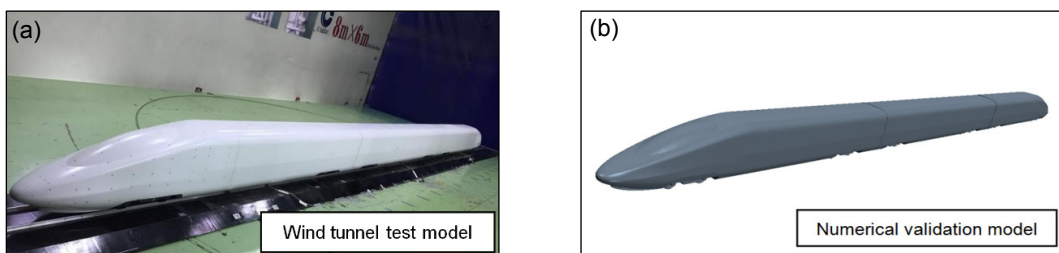


**Fig. 8 Train models used in wind tunnel test (a) and numerical validation (b)**

in the CFD validation are the same as those described in Sections 4.1–4.3. The DES method is used to predict the aerodynamic forces on the train. Table 3 shows the time-averaged aerodynamic coefficients for each coach of the HST predicted by the wind tunnel test and the numerical simulation. It can be seen that in Table 3, the differences in the drag

coefficients obtained by the numerical simulation and the wind tunnel test are within 2.07%, the maximum difference of the lift coefficient is 8.33% and is located at the middle coach, and the difference of the lift coefficient of the tail coach is 3.19%. The discrepancy is believed to be attributed to the difference in ground simulation between the numerical simulation and the

**Table 3 Comparison of aerodynamic coefficients predicted by wind tunnel test and numerical simulation**

Method	Head coach		Middle coach		Tail coach	
	$C_d$	$C_l$	$C_d$	$C_l$	$C_d$	$C_l$
Wind tunnel test	0.143	-0.045	0.070	-0.012	0.158	0.094
Numerical simulation	0.145	-0.047	0.071	-0.013	0.162	0.091
Error (%)	1.40	4.44	1.43	8.33	2.07	3.19

wind tunnel test. Thus, the mesh layout and numerical method used in the present paper are regarded as efficient in predicting the aerodynamic forces on HSTs.

## 5 Kriging model construction and prediction accuracy analysis

### 5.1 Description of the Kriging model

The Kriging model is an interpolation technique for spatially and temporally correlated data based on statistical theory (Oliver and Webster, 1990). This model combines a global model with the localized departure as formulated by

$$y(x) = f(x) + z(x), \quad (9)$$

where  $y(x)$  is the unknown function of interest,  $f(x)$  is a known polynomial function, and  $z(x)$  is the correlation function which is a realization of a stochastic process with mean zero and variance  $\sigma^2$ , and non-zero covariance. The term  $f(x)$  provides a global approximation of the design space, and the term  $z(x)$  creates localized deviations. The covariance matrix of  $z(x)$  is given by

$$\text{Cov}[z(x^i), z(x^j)] = \sigma^2 \mathbf{R}[R(\theta, x^i, x^j)], \quad (10)$$

$$i, j = 1, 2, \dots, n_s,$$

where  $n_s$  is the number of sample points,  $\mathbf{R}$  is the correlation matrix, and  $R(\theta, x^i, x^j)$  is the correlation function between any two of the sample points. The correlation function  $R$  would be specified by a user, and the Gaussian function is used:

$$R(\theta, x^i, x^j) = \exp\left[-\sum_{k=1}^m \theta_k |x_k^i - x_k^j|^2\right], \quad (11)$$

$$i, j = 1, 2, \dots, n_s,$$

where  $m$  is the number of the design variables,  $\theta_k$  are unknown correlation parameters used to fit the Kriging model, and  $x_k^i$  and  $x_k^j$  are the  $k$ th components of sample points  $x^i$  and  $x^j$ , respectively.

The essence of the construction of a Kriging model is to find the optimal values of  $\theta_k$  for the correlation function. To improve the prediction accuracy of a Kriging model, the mean of the prediction error must be zero, and the mean square error of the prediction error must be at a minimum. The optimal values of  $\theta_k$  can be obtained by solving Eq. (12) (Lee and Kim, 2007; Yao *et al.*, 2012b):

$$\text{Minimise } \varphi(\theta_k) = \frac{n_s}{2} \ln(\hat{\sigma}^2) + \frac{1}{2} \ln(|R|), \quad (12)$$

$$\text{Subject to: } \theta_k > 0,$$

where both  $\hat{\sigma}^2$  and  $|R|$  are functions of  $\theta_k$ .

### 5.2 Design of experiments

The sampling plan is called the design of experiments (DOE) which is used to fit the parameters of the Kriging model. In classical designs, random variations are considered. However, the classical designs are useless for deterministic computer experiments which do not have random errors. Therefore, it is more appropriate for computer experiments to fill the design space equally. As the optimal LHS plan is uniformly distributed over all variable dimensions and can ensure the sampling points represent the whole part of the design space without considering the dimension of the problem, 41 initial samples are obtained by the optimal LHS plan in this study. The top 40 samples are chosen as the initial training samples for the construction of the Kriging model, and the last one is chosen as the testing sample. The initial samples and their aerodynamic responses are shown in Table 4.

### 5.3 Construction of the Kriging model

To find the best Kriging model, the DACE Matlab Kriging toolbox is used to construct the Kriging model. The optimization method in the original DACE Matlab Kriging toolbox is a schema search method which is heavily dependent on the initial points (Lophaven *et al.*, 2002). To overcome that disadvantage, the GA is adopted in this paper as the optimization method in searching for the optimal values of  $\theta_k$  in Eq. (12). The initial population number is 100, and the evolution generation is 15. The probabilities of crossover and mutation are set to be 0.9 and 0.1, respectively.

Table 5 shows the prediction error for the testing sample point and the points selected from the Pareto front. In order to meet the engineering design requirements, the prediction accuracies of the optimization objectives are set as follows: the error of the total aerodynamic drag force is less than 1%, and the error of the aerodynamic lift force of the tail coach is less than 5%. It can be seen that in Table 5, after twice adding training points, the prediction accuracies of the testing sample points and the Pareto front points all meet the engineering requirements.

## 6 Results and discussion

### 6.1 Comparative study between the original train and an optimal train without crosswind

In the present paper, NSGA-II is selected as the optimization algorithm for the HST head; it is a

widely used multi-objective optimization method. This algorithm proposes a fast non-dominated sorting approach with an elitist strategy, and replaces the sharing function approach with a crowd-comparison approach, which does not need to define any parameter to maintain diversity among population members. The optimization process of NSGA-II includes selection, crossover, and mutation. The manners of crossover and mutation of NSGA-II are the same as those of the standard genetic operation. The parameters of the NSGA-II are set as follows: the initial population size is 50, the number of the evolution generation is 30, and the crossover probability is 0.9. A series of Pareto-optimal head shapes is obtained after the multi-objective optimization. Fig. 9 shows the Pareto front of the two optimization objectives. An optimal head shape is chosen for comparative study with the original head shape, as the square symbol shows in Fig. 9. The values of the design variables and optimization objectives for the original train and the optimal train are summarized in Table 6. After optimization, the total aerodynamic drag coefficient decreases by 2.61%, and the aerodynamic lift coefficient of the tail coach decreases by 9.90%. Compared with the original head shape, the nose height is increased by 19.8 mm (the original nose height is 764 mm), the top height of the front hood is increased by 15.4 mm, the angle of the cab window is increased by 4.25°, the lateral width of maximum horizontal control curve is narrowed with a maximal value of 30 mm, the concave degree of the auxiliary control curve in the middle of the streamlined head

**Table 4 Initial samples and their aerodynamic responses**

Type	No.	zs <sub>1</sub>	dz <sub>2</sub> (mm)	dz <sub>3</sub> (mm)	dy <sub>4</sub> (mm)	ys <sub>5</sub>	dy <sub>6</sub> (mm)	xs <sub>7</sub>	C <sub>d</sub> -total	C <sub>l</sub> -tail
	1	1.000	0.0	0.0	0.0	0.000	0.0	1.000	0.3371	0.0939
	2	1.108	112.8	71.8	-15.6	-0.185	12.3	0.526	0.3368	0.0845
	3	0.913	164.1	184.6	-3.3	0.169	23.1	1.372	0.3533	0.0993
	4	0.974	97.4	107.7	48.0	0.354	20.8	1.423	0.3548	0.1025
	5	0.944	194.9	66.7	31.5	-0.031	17.7	0.577	0.3331	0.0975
	6	1.159	56.4	164.1	-1.3	0.308	24.6	1.141	0.3525	0.0996
	7	1.015	184.6	30.8	2.8	-0.138	3.9	1.167	0.3443	0.0911
Training sample	8	1.077	153.9	153.9	-9.5	0.077	30.0	0.603	0.3404	0.0909
	...	...	...	...	...	...	...	...	...	...
	35	0.964	138.5	0.0	27.4	0.015	27.7	1.269	0.3488	0.0889
	36	1.108	71.8	35.9	45.9	-0.108	8.5	0.859	0.3327	0.0964
	37	1.169	169.2	15.4	-7.4	0.215	20.0	0.910	0.3370	0.0847
	38	1.056	25.6	179.5	31.5	-0.077	13.9	1.321	0.3418	0.0963
	39	0.800	118.0	118.0	21.3	-0.200	18.5	1.192	0.3405	0.0930
	40	1.149	10.3	10.3	11.0	0.138	21.5	1.218	0.3421	0.0954
Testing sample	41	0.954	41.0	194.9	-28.0	-0.062	19.2	0.885	0.3403	0.0936

reaches its maximum, the lateral width of the bogie area remains unchanged, and the partition angle of the bogie area is decreased to its minimum. The head shapes of the original train and the optimal train are shown in Fig. 10.

Table 7 shows the aerodynamic coefficients of different parts of the original train and the optimal train in conditions without crosswind. It can be seen that in Table 7, there are large variations in the inviscid drag forces of HSTs before and after optimization, and significant reductions of the inviscid drag forces exist in the head-nose and the bogie 1 which is beneath the streamlined head of the head coach. There are little variations in the viscous drag forces. Compared with the original train, the total inviscid drag force of the optimal train is reduced by 3.33%, the total viscous drag force is slightly increased by 0.21%, and the lift force of the tail coach is reduced by 9.90%.

**6.2 Comparative study between the original train and the optimal train under crosswinds**

Strong crosswind is frequently met by HSTs running in the open air, and the aerodynamic performance of HSTs under crosswinds will be much

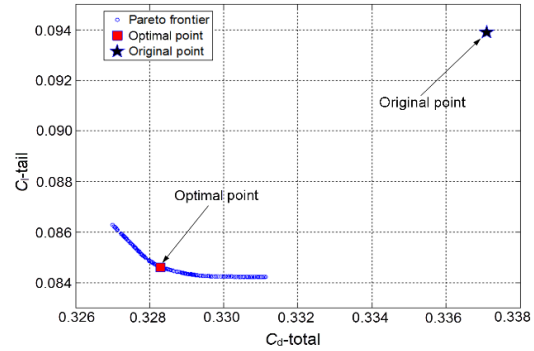


**Fig. 9 Pareto front based on the total  $C_d$  and  $C_l$  of the tail coach**

**Table 5 Prediction accuracy analysis of the Kriging model**

Adding time	Test point	$C_d$ -prediction	$C_d$ -CFD	$C_d$ -error (%)	$C_l$ -prediction	$C_l$ -CFD	$C_l$ -error (%)
1	Sample point	0.3386	0.3403	-0.49	0.0890	0.0936	-4.93
	Pareto front point 1	0.3305	0.3327	-0.65	0.0797	0.0906	-12.01
	Pareto front point 2	0.3282	0.3276	0.20	0.0845	0.0882	-4.24
2	Sample point	0.3387	0.3403	-0.46	0.0895	0.0936	-4.43
	Pareto front point 1	0.3316	0.3300	0.49	0.0803	0.0826	-2.81
	Pareto front point 2	0.3277	0.3283	-0.19	0.0879	0.0846	3.94

**Table 6 Values of design variables and optimization objectives of the original train and the optimal train**

Model	$zs_1$	$dz_2$ (mm)	$dz_3$ (mm)	$dy_4$ (mm)	$ys_5$	$dy_6$ (mm)	$xs_7$	$C_d$ -total	$C_l$ -tail
Original train	1.000	0.0	0.0	0.0	0.0	0.0	1.0	0.3371	0.0939
Optimal train	1.026	15.4	47.1	-30.0	-0.2	0.3	0.5	0.3283	0.0846
Reduction (%)	-	-	-	-	-	-	-	2.61	9.90

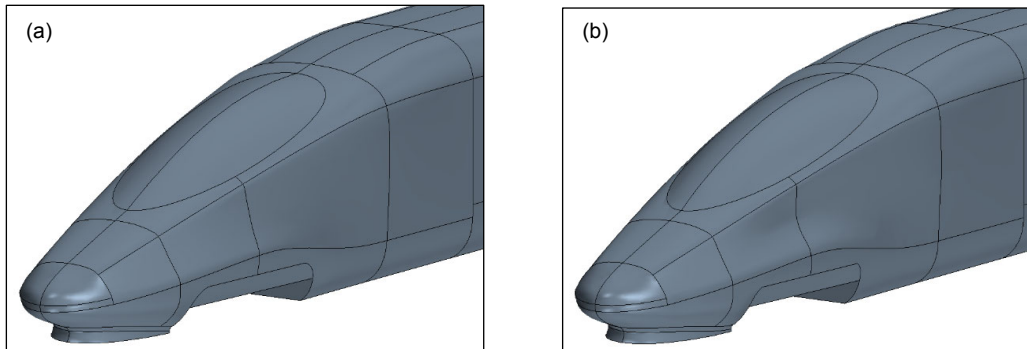


**Fig. 10 Head shapes of the original train (a) and the optimal train (b)**

lowered compared with that in conditions without a crosswind (Xiao *et al.*, 2014; Zhai *et al.*, 2015). Therefore, it is necessary to validate the feasibility of the optimal head shape in crosswind conditions. In the crosswind study, the running speed of the train is 350 km/h, the crosswind velocity is 15 m/s, and the crosswind direction is perpendicular to the train running direction. The mesh configuration and CFD method are the same as those in conditions without crosswind, except that a mesh refinement zone is defined in the leeward side of the train to precisely capture the vortex structures there. The total amount of the computational mesh in crosswind conditions is about 42.13 million.

As the aerodynamic performance of the head coach is the worst among the three coaches in crosswinds (Li *et al.*, 2013; Zhai *et al.*, 2015; Zhang *et al.*, 2016), the aerodynamic loads of the head coach as well as the total aerodynamic drag forces are analyzed. Table 8 is the time-averaged values of the unsteady aerodynamic coefficients before and after optimization.

Compared with the original train, the total aerodynamic drag coefficient ( $C_{d-total}$ ) is reduced by 2.98%, the lift coefficient of the head coach ( $C_l-head$ ) is increased by 5.30%, the side force coefficient of the head coach ( $C_s-head$ ) is slightly reduced by 0.24%, the absolute values of the overturning moment coefficient ( $C_{Mx-head}$ ) and the yawing moment coefficient ( $C_{My-head}$ ) of the head coach are increased by 1.08% and 2.99%, respectively, and the absolute value of the pitching moment coefficient ( $C_{Mz-head}$ ) is reduced by 8.75%.

Fig. 11 shows the time history of the aerodynamic coefficients of the head coach as well as the total aerodynamic drag coefficients for the trains before and after optimization. The amplitudes of  $C_{d-total}$ ,  $C_l-head$ ,  $C_s-head$ ,  $C_{Mx-head}$ ,  $C_{My-head}$ , and  $C_{Mz-head}$  of the original train are 0.0504, 0.0449, 0.0409, 0.0201, 0.0929, and 0.0651, respectively, while the amplitudes of the  $C_{d-total}$ ,  $C_l-head$ ,  $C_s-head$ ,  $C_{Mx-head}$ ,  $C_{My-head}$ , and  $C_{Mz-head}$  of the optimal train change to 0.0236, 0.0199, 0.0155, 0.0086,

**Table 7 Aerodynamic coefficients of different parts of the original train and the optimal train**

Train part	Original shape			Optimal shape		
	$C_{d-pressure}$	$C_{d-shear}$	$C_l-tail$	$C_{d-pressure}$	$C_{d-shear}$	$C_l-tail$
Head-nose	0.0324	0.0147	–	0.0299	0.0148	–
Head-body	0.0083	0.0138	–	0.0087	0.0139	–
Bogie 1	0.0576	0.0024	–	0.0550	0.0025	–
Bogie 2	0.0195	0.0012	–	0.0191	0.0010	–
Head-shield	0.0318	–0.0005	–	0.0319	–0.0005	–
Mid-body	0.0102	0.0186	–	0.0099	0.0186	–
Bogie 3	0.0095	0.0007	–	0.0082	0.0005	–
Bogie 4	0.0062	0.0005	–	0.0061	0.0004	–
Tail-shield	0.0283	–0.0004	–	0.0285	–0.0004	–
Bogie 5	0.0052	0.0003	–	0.0045	0.0003	–
Bogie 6	0.0051	0.0003	–	0.0049	0.0003	–
Tail-nose	0.0506	0.0076	0.0974	0.0495	0.0078	0.0954
Tail-body	0.0036	0.0098	–0.0034	0.0031	0.0100	–0.0108
Total	0.2682	0.0689	0.0939	0.2593	0.0691	0.0846
Reduction (%)	–	–	–	3.33	–0.21	9.90

**Table 8 Time-averaged values of the unsteady aerodynamic coefficients before and after optimization**

Model	$C_{d-total}$	$C_l-head$	$C_s-head$	$C_{Mx-head}$	$C_{My-head}$	$C_{Mz-head}$
Original	0.6207	0.3219	0.6412	–0.3880	–0.7720	–0.7837
Optimal	0.6022	0.3389	0.6397	–0.3922	–0.7045	–0.8071
Reduction (%)	2.98	–5.30	0.24	–1.08	8.75	–2.99

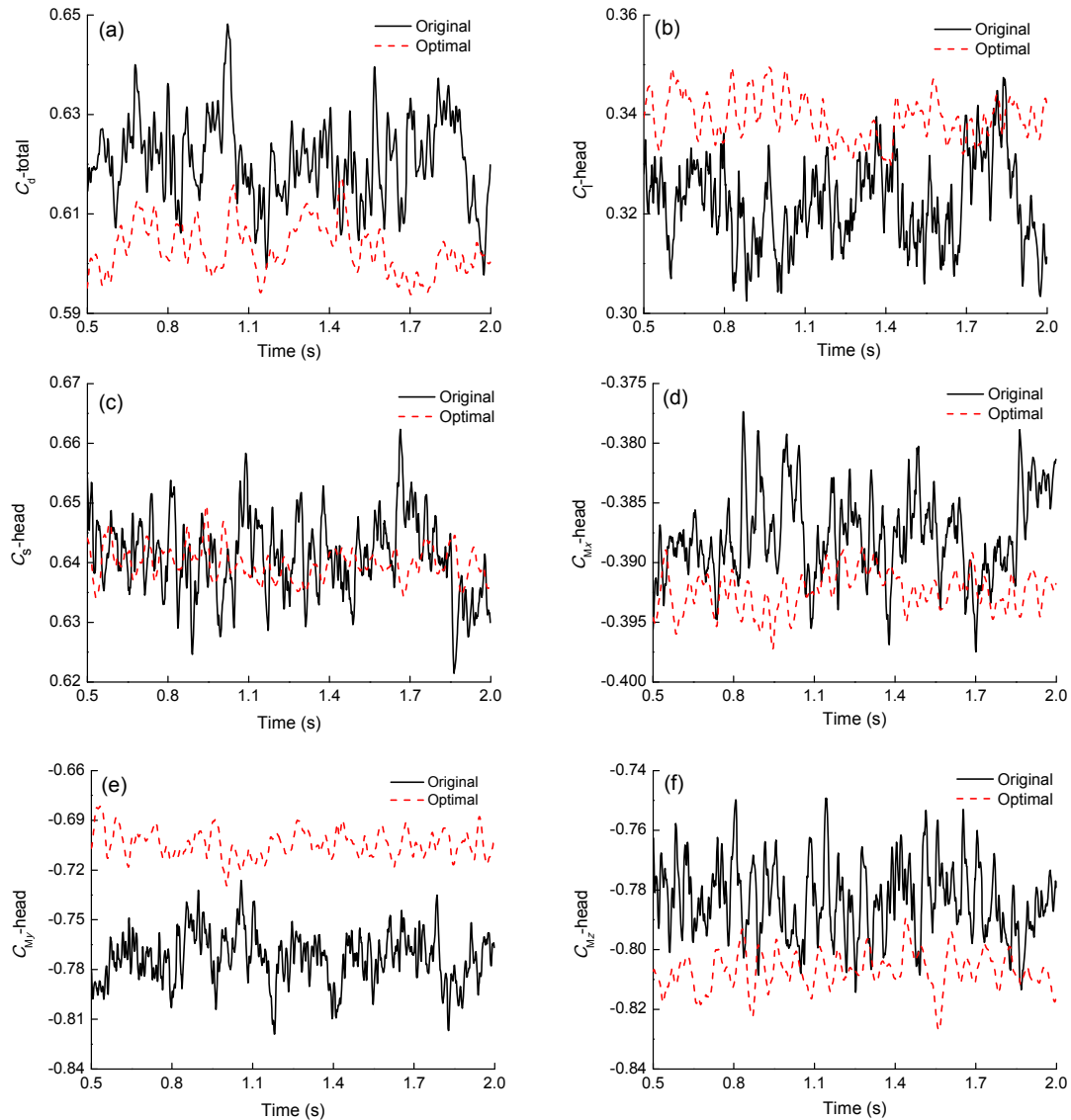


**Fig. 11** Time histories of  $C_d$ -total (a),  $C_l$ -head (b),  $C_s$ -head (c),  $C_{M_x}$ -head (d),  $C_{M_y}$ -head (e), and  $C_{M_z}$ -head (f) in crosswind conditions before and after optimization

0.0480, and 0.0377, respectively. Therefore, it can be concluded that the optimal train benefits from lower fluctuations of aerodynamic loads in crosswind conditions, which will be favorable for operational safety and comfort.

## 7 Conclusions

A multi-objective aerodynamic optimization design method of a HST head shape is presented in this paper. A parametric model of the HST head was

established and seven design variables of the head shape were studied. The multi-objective aerodynamic optimization design of the HST head shape combining NSGA-II and a Kriging model was performed, taking the total aerodynamic drag force and the lift force of the tail coach as the optimization objectives. After optimization, a series of Pareto-optimal head shapes was obtained. An optimal head shape was selected from the Pareto-optimal head shapes, and the aerodynamic performance of the HST with the optimal head shape was compared with that of the original train in conditions with and without crosswinds.

The results show that in conditions without crosswind, compared with the original train, the total aerodynamic drag force of the optimal train is reduced by 2.61%, and the aerodynamic lift force of the tail coach is reduced by 9.90%. In crosswind conditions, the total aerodynamic drag force of the optimal train is reduced by 2.98% and the aerodynamic side force of the head coach is slightly reduced by 0.24%. In addition, the HST with the optimal head benefits from low fluctuations of the aerodynamic loads in crosswind conditions.

## References

- Baker, C., 2010. The flow around high speed trains. *Journal of Wind Engineering and Industrial Aerodynamics*, **98**(6-7): 277-298.  
<http://dx.doi.org/10.1016/j.jweia.2009.11.002>
- Bell, J.R., Burton, D., Thompson, M.C., et al., 2015. Moving model analysis of the slipstream and wake of a high-speed train. *Journal of Wind Engineering and Industrial Aerodynamics*, **136**:127-137.  
<http://dx.doi.org/10.1016/j.jweia.2014.09.007>
- Brockie, N.J.W., Baker, C.J., 1990. The aerodynamic drag of high speed trains. *Journal of Wind Engineering and Industrial Aerodynamics*, **34**(3):273-290.  
[http://dx.doi.org/10.1016/0167-6105\(90\)90156-7](http://dx.doi.org/10.1016/0167-6105(90)90156-7)
- Ding, S.S., Li, Q., Tian, A.Q., et al., 2016. Aerodynamic design on high-speed trains. *Acta Mechanica Sinica*, **32**(2):215-232.  
<http://dx.doi.org/10.1007/s10409-015-0546-y>
- Eichinger, S., Sima, M., Thiele, F., 2015. Numerical simulation of a regional train in cross-wind. *Proceedings of the Institution of Mechanical Engineers, Part F: Journal of Rail and Rapid Transit*, **229**(6):625-634.  
<http://dx.doi.org/10.1177/0954409714555383>
- Han, J., Zhao, G.T., Xiao, X.B., et al., 2015. Effect of softening of cement asphalt mortar on vehicle operation safety and track dynamics. *Journal of Zhejiang University-SCIENCE A (Applied Physics & Engineering)*, **16**(12):976-986.  
<https://dx.doi.org/10.1631/jzus.A1500080>
- Krajnović, S., 2009. Shape optimization of high-speed trains for improved aerodynamic performance. *Proceedings of the Institution of Mechanical Engineers, Part F: Journal of Rail and Rapid Transit*, **223**(5):439-452.  
<http://dx.doi.org/10.1243/09544097JRRT251>
- Lee, J., Kim, J., 2007. Kriging-based approximate optimization of high-speed train nose shape for reducing micro-pressure wave. *Proceedings of the Institution of Mechanical Engineers, Part F: Journal of Rail and Rapid Transit*, **221**(2):263-270.  
<http://dx.doi.org/10.1243/09544097JRRT110>
- Li, R., Xu, P., Peng, Y., et al., 2016. Multi-objective optimization of a high-speed train head based on the FFD method. *Journal of Wind Engineering and Industrial Aerodynamics*, **152**:41-49.  
<http://dx.doi.org/10.1016/j.jweia.2016.03.003>
- Li, T., Zhang, J.Y., Zhang, W.H., 2013. A numerical approach to the interaction between airflow and a high-speed train subjected to crosswind. *Journal of Zhejiang University-SCIENCE A (Applied Physics & Engineering)*, **14**(7): 482-493.  
<http://dx.doi.org/10.1631/jzus.A1300035>
- Lophaven, S.N., Nielsen, H.B., Sondergaard, J., 2002. DACE-A Matlab Kriging Toolbox, Version 2.0.
- Muñoz-paniagua, J., Garcia, J., Crespo, A., 2014. Genetically aerodynamic optimization of the nose shape of a high-speed train entering a tunnel. *Journal of Wind Engineering and Industrial Aerodynamics*, **130**:48-61.  
<http://dx.doi.org/10.1016/j.jweia.2014.03.005>
- Nishino, T., Roberts, G.T., Zhang, X., 2008. Unsteady RANS and detached-eddy simulations of flow around a circular cylinder in ground effect. *Journal of Fluids and Structures*, **24**(1):18-33.  
<http://dx.doi.org/10.1016/j.jfluidstructs.2007.06.002>
- Oliver, M.A., Webster, R., 1990. Kriging: a method of interpolation for geographical information systems. *International Journal of Geographical Information System*, **4**(3): 313-332.  
<http://dx.doi.org/10.1080/02693799008941549>
- Ragunathan, R.S., Kim, H.D., Setoguchi, T., 2002. Aerodynamics of high-speed railway train. *Progress in Aerospace Sciences*, **38**(6-7):469-514.  
[http://dx.doi.org/10.1016/S0376-0421\(02\)00029-5](http://dx.doi.org/10.1016/S0376-0421(02)00029-5)
- Schwanitz, S., Wittkowski, M., Rolny, V., et al., 2013. Pressure variations on a train: where is the threshold to railway passenger discomfort? *Applied Ergonomics*, **44**(2): 200-209.  
<http://dx.doi.org/10.1016/j.apergo.2012.07.003>
- Smith, R.A., Zhou, J., 2014. Background of recent developments of passenger railways in China, the UK and other European countries. *Journal of Zhejiang University-SCIENCE A (Applied Physics & Engineering)*, **15**(12): 925-935.  
<http://dx.doi.org/10.1631/jzus.A1400295>
- Sone, S., 2015. Comparison of the technologies of the Japanese Shinkansen and Chinese High-speed Railways. *Journal of Zhejiang University-SCIENCE A (Applied Physics & Engineering)*, **16**(10):769-780.  
<http://dx.doi.org/10.1631/jzus.A1500220>
- Sun, Z.X., Song, J.J., An, Y.R., 2010. Optimization of the head shape of the CRH3 high speed train. *Science China Technological Science*, **53**(12):3356-3364.  
<http://dx.doi.org/10.1007/s11431-010-4163-5>
- Tan, P., Ma, J.E., Zhou, J., et al., 2016. Sustainability development strategy of China's high speed rail. *Journal of Zhejiang University-SCIENCE A (Applied Physics & Engineering)*, **17**(12):923-932.  
<http://dx.doi.org/10.1631/jzus.A1600747>
- Thompson, D.J., Iglesias, E.L., Liu, X.W., et al., 2015. Recent developments in the prediction and control of aerodynamic noise from high-speed trains. *International Journal*

- of Rail Transportation, **3**(3):119-150.  
<http://dx.doi.org/10.1080/23248378.2015.1052996>
- Vytla, V.V., Huang, P.G., Penmetsa, R.C., 2010. Multi objective aerodynamic shape optimization of high speed train nose using adaptive surrogate model. Proceedings of the 28th AIAA Applied Aerodynamic Conference, p.23-26.
- Xiao, X.B., Ling, L., Xiong, J.Y., et al., 2014. Study on the safety of operating high-speed railway vehicles subjected to crosswinds. *Journal of Zhejiang University-SCIENCE A (Applied Physics & Engineering)*, **15**(9):694-710.  
<http://dx.doi.org/10.1631/jzus.A1400062>
- Yang, G.W., Guo, D.L., Yao, S.B., et al., 2012. Aerodynamic design for China new high-speed trains. *Science China Technological Sciences*, **55**(7):1923-1928.  
<http://dx.doi.org/10.1007/s11431-012-4863-0>
- Yao, S.B., Guo, D.L., Yang, G.W., et al., 2012a. Distribution of high-speed train aerodynamic drag. *Journal of the China Railway Society*, **34**(7):18-23 (in Chinese).
- Yao, S.B., Guo, D.L., Sun, Z.X., et al., 2012b. Multi-objective optimization of the streamlined head of high-speed trains based on the Kriging model. *Science China Technological Science*, **55**(12):3495-3509.  
<http://dx.doi.org/10.1007/s11431-012-5038-8>
- Yao, S.B., Guo, D.L., Sun, Z.X., et al., 2014. Optimization design for aerodynamic elements of high speed trains. *Computers & Fluids*, **95**(3):56-73.
- Yao, S.B., Guo, D.L., Sun, Z.X., et al., 2016. Parametric design and optimization of high speed train nose. *Optimization and Engineering*, **17**(3):605-630.  
<http://dx.doi.org/10.1007/s11081-015-9298-6>
- Yu, M.G., Zhang, J.Y., Zhang, W.H., 2013. Multi-objective optimization design method of the high-speed train head. *Journal of Zhejiang University-SCIENCE A (Applied Physics & Engineering)*, **14**(9):631-641.  
<http://dx.doi.org/10.1631/jzus.A1300109>
- Zhai, W.M., Yang, J.Z., Li, Z., et al., 2015. Dynamics of high-speed train in crosswinds based on an air-train-track interaction model. *Wind and Structures*, **20**(2):143-168.  
<http://dx.doi.org/10.12989/was.2015.20.2.143>
- Zhang, L., Zhang, J.Y., Li, T., et al., 2016. Unsteady aerodynamic characteristics and safety of high-speed trains under crosswinds. *Journal of Mechanical Engineering*, **52**(6):124-135 (in Chinese).  
<http://dx.doi.org/10.3901/JME.2016.06.124>
- Zhang, Z.Z., Zhou, D., 2013. Wind tunnel experiment on aerodynamic characteristic of streamline head of high speed train with different head shapes. *Journal of Central South University (Science and Technology)*, **44**(6):2603-2608 (in Chinese).  
[http://dx.doi.org/1672-7207\(2013\)06-2603-06](http://dx.doi.org/1672-7207(2013)06-2603-06)

## 中文概要

**题目:** 高速列车头部外形多目标气动优化设计

**目的:** 为改善高速列车明线运行时的气动性能, 提出一种基于近似模型的高速列车头部外形多目标气动优化设计方法。

**创新点:** 1. 建立包含转向架区域的高速列车参数化模型; 2. 基于近似模型并结合遗传算法, 对高速列车头部外形及转向架区域进行多目标气动优化设计。

**方法:** 1. 建立包含转向架区域的原始头型高速列车模型(图2和3), 并基于CATIA脚本文件和MATLAB自编程序对列车头部外形进行参数化处理; 2. 通过最优拉丁超立方设计方法在设计空间内对优化设计变量进行采样, 并采用计算流体力学方法对样本点中新头型列车气动性能进行计算; 3. 基于样本点的列车头型优化设计变量及优化目标(表4), 建立优化目标与设计变量之间的近似模型; 4. 基于近似模型和多目标遗传算法, 对高速列车头部外形进行多目标优化设计, 选取其中的一个优化头型与原始头型进行比较, 并验证横风下优化头型的可行性。

**结论:** 1. 相较于原始头型列车, 无横风时, 优化头型列车的整车气动阻力减小 2.61%, 尾车气动升力减小 9.90%; 2. 横风下, 优化头型列车的整车气动阻力减小 2.98%, 头车气动侧力减小 0.24%; 3. 横风下, 优化头型列车的头车气动载荷波动幅值有所减小。

**关键词:** 高速列车; 多目标优化; 气动性能; 参数化模型; 克里格模型; 遗传算法